

Wright State University

CORE Scholar

[Browse all Theses and Dissertations](#)

[Theses and Dissertations](#)

2009

Sub-mm Wave Imaging and Waveguiding Techniques for Non-Destructive Materials Evaluation

Izaak Vincent Kemp
Wright State University

Follow this and additional works at: https://corescholar.libraries.wright.edu/etd_all



Part of the [Physics Commons](#)

Repository Citation

Kemp, Izaak Vincent, "Sub-mm Wave Imaging and Waveguiding Techniques for Non-Destructive Materials Evaluation" (2009). *Browse all Theses and Dissertations*. 960.
https://corescholar.libraries.wright.edu/etd_all/960

This Thesis is brought to you for free and open access by the Theses and Dissertations at CORE Scholar. It has been accepted for inclusion in Browse all Theses and Dissertations by an authorized administrator of CORE Scholar. For more information, please contact library-corescholar@wright.edu.

SUB-MM WAVE IMAGING AND WAVEGUIDING

TECHNIQUES FOR NON-DESTRUCTIVE

MATERIALS EVALUATION

A thesis submitted in partial fulfillment
of the requirements for the degree of
Master of Science

By

IZAAK VINCENT KEMP
B.S., University of Cincinnati, 2007

2009
Wright State University

WRIGHT STATE UNIVERSITY
SCHOOL OF GRADUATE STUDIES

August 21, 2009

I HEREBY RECOMMEND THAT THE THESIS PREPARED
UNDER MY SUPERVISION BY Izaak Vincent Kemp
ENTITLED Sub-mm Wave Imaging and Waveguiding
Techniques for Non-Destructive Materials
Evaluation BE ACCEPTED IN PARTIAL FULFILLMENT
OF THE REQUIREMENTS FOR THE DEGREE OF Master
of Science.

Doug Petkie, Ph.D.
Thesis Director

Lok Lew Yan Voon, Ph.D.
Department Chair

Committee on
Final Examination

Doug Petkie, Ph.D.

Jason Deibel, Ph.D.

Jerry Clark, Ph.D.

Joseph F. Thomas, Jr., Ph.D.
Dean, School of Graduate Studies

Abstract

Kemp, Izaak V., M.S., Department of Physics, Wright State University, 2009. Sub-mm Wave Imaging and Waveguiding Techniques for Non-Destructive Materials Evaluation.

Sub-mm wave technology (also known as Terahertz/THz) is a rapidly developing field of electro-optics which has great potential in a variety of applications. Generally defined as the band of the electro-magnetic spectrum with frequencies spanning from 300 GHz to 30 THz, sub-mm waves are non-ionizing and are capable of passing through a wide range of dielectric substances making them well suited for imaging purposes such as non-destructive materials evaluation (NDE). Because of their high sensitivity to metals and ability to penetrate surface obscuring materials such as paint, oil, and epoxy sub-mm waves are capable of imaging corrosion damage on metallic surfaces as well as burn damage in composites routinely used in aerospace structures, with resolution comparable to many of the currently employed NDE techniques. In order to avoid failure of components during operation, many aircraft parts are replaced earlier than necessary leading to higher costs that could be reduced if the degree of damage in the component material could be determined non-destructively without requiring contact with the section to be imaged, thus a portable real-time sub-mm wave imaging system if developed would possess significant promise in the NDE market. We have developed a sub-mm wave imaging system and have compiled a library of images which successfully demonstrate the potential of such a system in evaluating aerospace materials.

However there are still many unsolved issues related to the propagation of sub-mm wave radiation that need to be addressed before a practical system can be produced for use in the field.

One major problem is that all of the substances which possess the refractive index profile and absorption coefficients necessary for the production of a sub-mm waveguide equivalent to fiber-optic cables are crystalline, making them impractical for use in NDE applications. Since the sub-mm wave imaging systems we have researched are active a practical NDE system would either need a compact source or a method of propagating sub-mm radiation over substantial distances to the sample to be imaged. One proposed method is the utilization of what are known as Sommerfield-Zenneck waves, or surface plasmon polaritons (SPPs). These surface electron density waves are capable of propagating over large distances and many metals possess SPP modes with frequencies in the sub-mm wave band. In addition to our NDE efforts, we have constructed a wire waveguide capable of exciting and transmitting these modes, and have characterized a number of its properties via imaging of the diffracted outgoing wave.

TABLE OF CONTENTS

Page

I. INTRODUCTION

1.1 Background.....	3
1.2 Terahertz imaging and non-destructive materials evaluation.....	5
1.3 Sub-mm cylindrical wire wave guides.....	7

II. EXPERIMENTAL THEORY AND PROCEDURE

2.1 Continuous sub-mm wave generation and detection.....	9
2.2 Scattering Theory.....	12
2.3 Sommerfeld-Zenneck surface wave theory.....	14
2.4 CW Sub-mm wave imaging procedure.....	18
2.5 Wire waveguide procedure.....	21
2.6 Software control.....	26
2.7 Image processing.....	28

III. NDE RESULTS

3.1 Evaluation of metallic samples.....	31
3.2 Evaluation of composite samples.....	35

IV. SOMMERFELD-ZENNECK WAVE RESULTS

4.1 Initial measurements and efficiency of coupling wire.....	39
4.2 Evaluation of outgoing wave as a function of distance.....	41

4.3 Evaluation of outgoing wave as a function of frequency.....	44
4.4 Effects of the presence of conductors on the outgoing wave.....	45
V. CONCLUSIONS.....	47
REFERENCES.....	48

LIST OF FIGURES

Figure	Page
1: Graph of electromagnetic technology advancements and THz gap.....	1
2: Image of sub-mm wave source and graph of output power vs. frequency.....	9
3: Cylindrical coordinate system and fields corresponding to SPP wave.....	14
4: FEM simulation of Sommerfeld-Zenneck wave.....	17
5: Schematic diagram of imaging system.....	18
6: Schematic diagram of wire waveguide experiment.....	21
7: Photos of wire waveguide setup.....	21
8: Image and line profile of copper wire results.....	22
9: Front panel of software control program.....	26
10: Example of image processing effects.....	28
11: Example of the effects of interpolation.....	29
12: Images of metallic sample A1R-004.....	31
13: Images of metallic sample C1R-001.....	32
14: Close up image and line profiles of metallic sample C1R-001.....	33
15: Images of composite sample KT-3.....	35
16: Images of composite sample KT-4.....	36
17: Images of composite sample NKT-4.....	37

18: 2D image of outgoing wave and corresponding line profile.....	41
19: 3D plot of outgoing intensity versus distance.....	42
20: Plots of peak-to-peak distance as a function of displacement.....	43
21: 3D plot of outgoing intensity as a function of frequency.....	44
22: 2D images of outgoing wave in the presence of a conductor.....	45

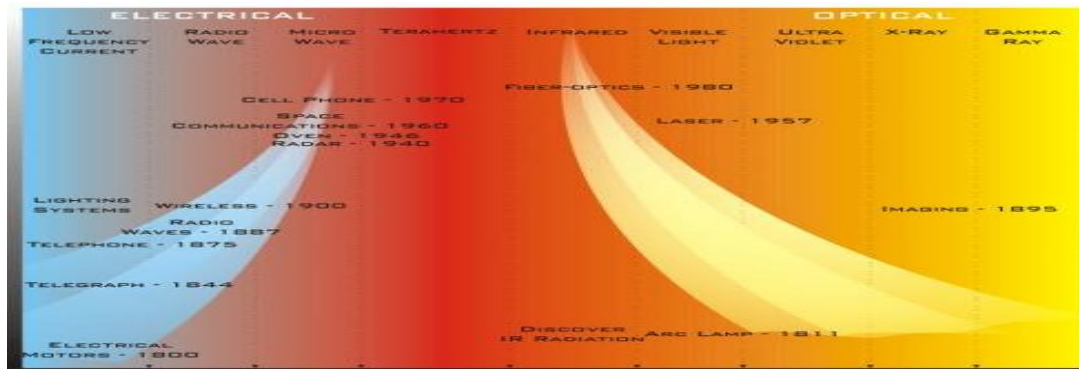


Figure 1: Graph illustrating the advancement of electromagnetic-wave technology and the so called “Terahertz gap”¹

I. Introduction

Sub-mm wave or Terahertz (THz) radiation is loosely defined as the region of the electromagnetic spectrum with frequencies ranging between 300 GHz and 30 THz (with corresponding wavelengths between 1mm and 10 μ m). This band is composed of frequencies within what is known as the “Terahertz gap”, the range of frequencies that fall between bands where radiation is typically generated by electronic devices (such as radio and microwave frequencies) and bands where radiation is usually created using optical techniques (see Figure 1). Although THz frequencies have been eagerly studied by astronomers for quite some time², only recently have advances in photonics allowed for the investigation of more earthbound applications. Because this research is relatively new, Terahertz radiation is known by a variety of different names within the scientific community including T-ray, sub-mm wave, and far IR. In this work we will refer to the band as either THz or sub-mm wave. Today, THz technology research has expanded to include a wide variety of functions: biomedical imaging, homeland security, environmental modeling, molecular spectroscopy, and non-destructive materials evaluation³. The motive for this preponderance of research is that the THz band possesses

many useful properties; THz radiation is non-ionizing meaning that it is non-destructive and safe for use on living tissue, many molecules possess resonant frequencies in the THz band making it particularly useful for spectroscopy, and THz radiation is capable of passing through a wide variety of dielectrics such as fabrics, paints, and dirt giving it great potential in a number of imaging applications⁴. In this thesis, we will explore the potential for sub-mm waves to be used as a means for non-destructive materials evaluation and will detail some experimental waveguide techniques with the potential to expand our already existing system.

1.1 Background

Aircraft components such as wings and fuselages are constantly exposed to harsh environments making them susceptible to corrosion initiation and growth. In order to ensure safe operation aircraft parts are routinely replaced before the end of their life-span which leads to higher costs, the US Air Force alone currently spends billions of dollars in preventative maintenance on aircraft,⁵ the cost of which could be reduced if a better method of evaluation were developed. Currently the US air force and major airlines employ ultrasound techniques to look for pitting and cracking due to corrosion, however these techniques require direct contact with the surface of the component part meaning they are only useable during an aircraft's 'tear-down' inspection, a lengthy process involving the disassembly of a large portion of the aircraft⁶. THz imaging has the potential to replace this technology as it is non-contact, has better resolution, and is not affected by surface dielectrics such as paint, oil, and epoxy commonly found on the surface of aircraft and is thus usable during routine inspection. Sub-mm waves also have the potential to image structural damage in composite materials such as polyamides which are becoming more and more predominant as primary aircraft structure materials. We have demonstrated that metallic corrosion and composite damage can be successfully imaged using THz, however there are still limitations to the practical use of THz in the field.

One of the major problems hindering the application of THz radiation is the lack of materials which exhibit the refractive index and absorption behavior necessary to make

fiber-optic waveguides. All of the materials whose properties are suited for THz fiber-optics are crystalline⁷ which limits their usefulness as transmission cable due to their fragility. One proposed method of THz propagation that seeks to overcome these challenges is the utilization of what are known both as Sommerfield-Zenneck waves or Surface-Plasmon-Polaritons (SPPs). These are surface electron density waves that can propagate over large distances, and many common metals such as copper and tungsten exhibit SPP modes at frequencies in the THz regime. In this thesis we present one proposed method of coupling linearly polarized THz radiation to these modes in cylindrical metal wires and discuss their potential applications as sub-mm wave transmission lines and for THz near-field imaging.

1.2 Terahertz Imaging and Non-Destructive Materials Evaluation (NDE)

The two main types of THz imaging systems currently being used today are known as continuous-wave systems (CW), which can be either *active* or *passive*, and Time-Domain-Systems (TDS), which are active. These two types of systems illustrate the opposing technological approaches which seek to bridge the THz gap. CW systems utilize a variety of technical schemes including diode-based frequency multipliers, backward wave oscillators, and free-electron lasers to either increase the frequency of an initial microwave signal, as fundamental oscillators, or down convert optical radiation to sub-mm wavelengths via photomixing. TDS systems on the other hand utilize ultra-fast optics and non-linear crystals to generate a single-cycle pulse with pulse widths on the order of picoseconds. Aside from the fundamental methods of detection and propagation, the main differences between TDS and CW imaging systems are size, cost, data complexity, and processing time⁸. CW imaging systems simply measure the power of the radiation scattered by the sample, while TDS systems are capable of measuring a variety of parameters including electric field magnitude, phase, and optical path length. While this makes TDS systems a more attractive experimental technique, the cost and size of TDS systems (at the time this thesis is written) make them impractical for routine evaluation of materials during maintenance inspections. In addition, passive sub-mm wave systems lack the signal to noise (SNR) requirements to provide good contrast for accurate grading of damage and defects⁹. For this reason we have focused our studies on active CW techniques as a method for materials evaluation.

Non-destructive materials evaluation (NDE) is, as the name implies, a method for evaluating the structure and composition of a component material that leaves the material intact and safe for continued use. NDE methods are routinely used in maintenance inspections of vehicles and aircraft and there are a wide variety of techniques used. Examples of currently implemented NDE technologies are pulse/echo ultrasound imaging, eddy current testing, thermographic inspection, and microradiography¹⁰. Each of these methods has its own set of advantages and disadvantages, but ultrasound is by far the most widely used method because of its relatively low cost and image processing time. Ultrasound techniques, however, require direct contact with the sample to be imaged and thus can only be used on active vehicles and aircraft during a ‘tear down’ inspection, as mentioned previously. Sub-mm wave systems are non-contact and can easily penetrate obscuring materials such as paint, oil, and epoxy commonly found on the surface of vehicles and thus could be utilized for more routine maintenance of vehicles. Sub-mm waves also boast advantages in terms of resolution compared to ultrasound, making them a more reliable method of evaluation. The tradeoff is that sub-mm wave systems are incapable of passing through metal and are thus incapable of subsurface imaging for metallic components, however many types of corrosion exhibit surface defects which are clearly identifiable to a trained technician.

1.3 Sub-mm Cylindrical Wire Wave Guides

The concept of surface electro-magnetic wave propagation along an infinitely long cylindrical wire of finite conductivity was first addressed by A. Sommerfeld in 1899 as a theoretical set of solutions to Maxwell's equations given the appropriate boundary conditions¹¹. The physical reality of these waves was long debated as the boundary conditions used by Sommerfeld required a conductor of infinite length and plane electro-magnetic waves, in other words the source of the radiation was required to be infinitely far removed from the cylindrical surface. Because Sommerfeld's cylindrical surface waves were similar in terms of boundary conditions to the solutions for ground wave propagation along the surface of the earth proposed by his student, J. Zenneck, they are referred to as Sommerfeld-Zenneck waves in the literature. However, while the existence and/or practicality of Zenneck's surface wave continues to be debated, it was experimentally verified that Sommerfeld's cylindrical surface waves could be generated with high enough efficiency to be employed for guided power transmission in the late 1940s. Goubau was the first to propose the use of these waves for transmission lines¹², but due to the advent of fiber-optic technology shortly thereafter the method was never fully realized.

Because standard waveguides and fiber-optic materials in the sub-mm wave band are impractical for field use due to their high attenuation or crystalline structure, interest in the use of Sommerfeld-Zenneck waves (also known as surface plasmon polaritons or SPPs for short) for transmission lines has resurfaced. Although exact analytical solutions to Maxwell's equations for the propagation of these modes across a conductor of finite

length are not known, several groups have been successful in developing numerical solutions based on finite-element analysis algorithms¹³. In addition a number of different techniques have been proposed and studied for efficiently coupling incoming linearly polarized sub-mm radiation to the radially polarized Sommerfeld-Zenneck modes of a cylindrical conductor¹⁴. All of the research conducted thus far on SPP waveguides has either been simulation or TDS experiments. To this author's knowledge no experiments have been performed with these waves using a CW system, and since CW systems have greater output power than TDS they are less affected by the relatively low coupling efficiencies involved in exciting these modes. By coupling outgoing sub-mm wave radiation to the SPP modes of metal wires one creates a wire waveguide capable of acting as a transmission line in the THz band, which has the potential to solve some of the problems inherent in creating a practical sub-mm wave imaging system for NDE use in the field, as well as having potential uses for sub-mm wave microscopy and near-field imaging. Although these investigations are very preliminary, they suggest a line of investigation which could prove significant in the transition of sub-mm wave technology from the lab to applications in the outside world.

II. Theory and Experimental Procedure

2.1 Continuous Sub-mm Wave Generation and Detection

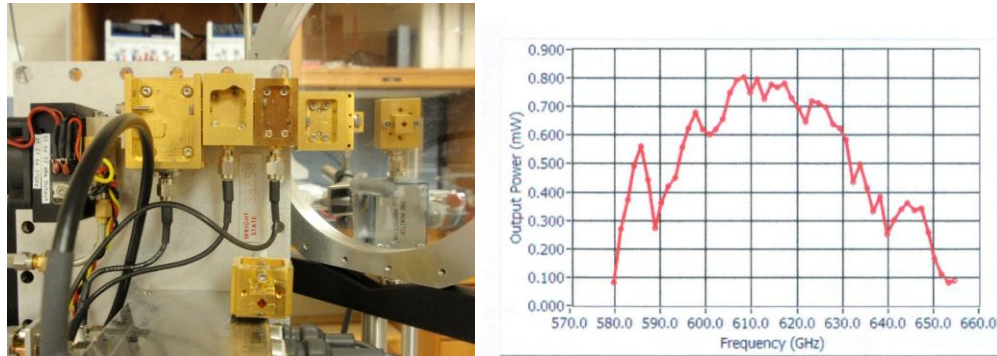


Figure 2: Images of Schottky diode chain and graph of its output power vs. frequency. The direct detector can be seen on the right in the picture, behind the beam-splitter.

As mentioned in the introduction, CW sub-mm wave systems typically begin with a signal in the microwave band and use frequency multiplication techniques to generate an outgoing wave in the sub-mm wave regime. In the case of our experiments microwave generation was achieved through the use of a YIG crystal oscillator contained within a commercial microwave synthesizer produced by the company Agilent. The outgoing microwave signal, between 6-15 GHz, was then transferred using co-axial cable to our frequency multiplication chain, another commercial system produced by Virginia Diodes Inc. (VDI). The frequency multiplication chain consists of a series of second and third harmonic multiplier diodes, known as Schottky Diodes, which generate the outgoing sub-mm wave radiation.

Conceptually, the frequency multiplication of microwaves is analogous to the harmonic generation of optical waves in a non-linear crystal. Within the frequency multiplier, Schottky diodes function as nonlinear media, converting the incoming microwaves into their harmonic waves. The Schottky diode consists of a metal-semiconductor junction, known as a Schottky barrier, where the semiconductor (usually GaAs) is monolithically fabricated on top of an ohmic metal. Though conceptually similar to a common p-n junction, Schottky barriers have much faster switching times (on the order of 100 picoseconds), allowing for the creation of higher frequency signals¹⁵. Although Schottky diodes tend to have low output power compared to other diode configurations (our system had an output of approximately 0.8 mW at 610 GHz), their output power is large when compared to other methods of generating sub-mm waves and can easily be detected. CW systems are also highly coherent, our system possessed a spectral linewidth of less than 1 kHz.

Our detection scheme employed a direct Schottky diode detector, also manufactured by VDI, which utilizes Schottky barriers to convert incoming sub-mm wave radiation into an electric voltage. The detector was capable of operating over the same range of frequencies as our source, with a peak responsivity of 1400 V/W at 610GHz. This output was then sent through a lock-in amplifier, which utilizes a technique known as phase-sensitive detection to filter out noise sources which in this case can be thousands of times larger than the signal¹⁶. The lock-in uses an external reference signal provided by the signal generator (amplitude modulation from the Agilent microwave generator) to reject noise which is not at the same frequency as the desired signal. The lock-in also amplifies the output, allowing for small differences in signal

intensity to be measured accurately. It should be noted that our detection scheme only measures the power of the incoming radiation, in other words it is not sensitive to electric field magnitude, phase, or optical path length. While this means that a great deal of information about the signal is lost, it also means that the system can collect data very quickly, with time-constants on the order of milliseconds.

2.2 Scattering Theory

Scattering refers to the physical process of the forced deviation of electromagnetic radiation from its trajectory as predicted by the law of reflection, caused by the inhomogeneous nature of the medium through which it travels. The three most well known types of scattering are Raman (inelastic), Mie-Debye, and Rayleigh (elastic) all of which have been extensively covered in the literature¹⁷; in the case of sub-mm waves interacting with aircraft materials Mie-Debye scattering is the most prominent since the size of the defects (scattering sources) are comparable to the wavelength of the radiation. Because of the importance of the Mie-Debye solution to understanding our NDE images it is briefly introduced herein.

The Debye solution assumes the incident material is a homogeneous and isotropic and that defects such as voids, cracks, and delaminations are of homogeneous spherical or cylindrical shape. For perpendicular incidence upon a cylindrical defect, the scattered wave will be polarized the same way as the incident radiation and propagate in the plane perpendicular to the cylinder's surface in the plane including the incident ray¹⁸. Radiation scattered in such a manner is likely to not be captured by the detector. The intensity of perpendicularly incident radiation (integrated over solid angle $d\Omega$) on a cylindrical defect is approximated by:

$$I = I_o \frac{\pi^4 a^4}{\lambda^3 r} (m^2 - 1)^2 \quad (1)$$

where I_o is the expected (non-scattered) intensity, a is the radius of the cylindrical defect, r is the distance between the detector and the center of the cylinder, and m is the ratio of the refractive indices (defect/medium). In the case of spherical defects, the intensity of perpendicularly incident radiation is approximated by:

$$I = I_o \frac{16\pi^4 a^6}{\lambda^4 r^2} \left(\frac{m^2 - 1}{m^2 + 2} \right)^2 \quad (2)$$

In both cases the reflected intensity is greatly reduced by the factors of r (which in our case is much larger than a and λ) and m (which can be roughly approximated as 1.4 for defects and 0.7 for voids) which means that sampled radiation in the area of defects will be decreased by orders of magnitude. The net effect is that defects will appear as dark spots in an image. Although the Mie-Debye solution takes different forms for non-perpendicular incidence and detection, these approximate solutions illustrate the fact that inconsistencies in an otherwise homogeneous medium will generally result in lowered reflected intensity, which for our purposes is sufficient.

2.3 Sommerfeld-Zenneck Surface Wave

Theory

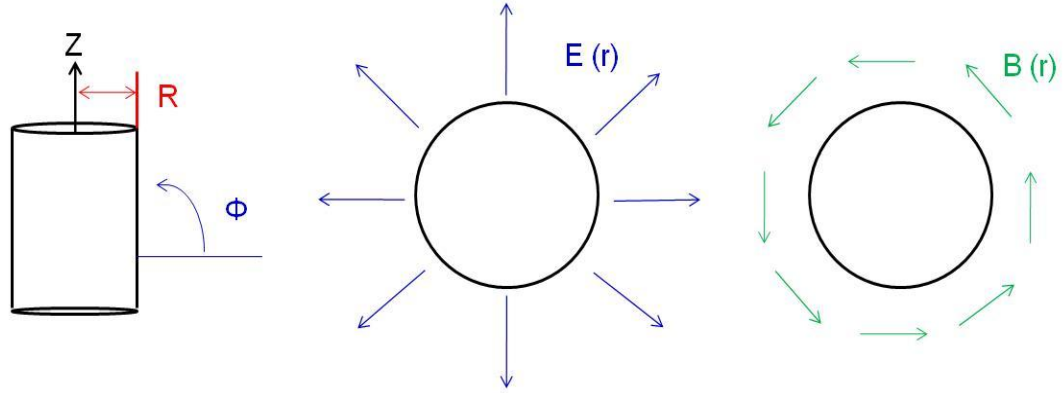


Figure 3: Graphical representation of a cylindrical coordinate system and the electric and magnetic fields of a Sommerfeld-Zenneck wave. The radially polarized field vectors are shown with respect to a transverse cross-section of the cylinder.

As mentioned above, it was Sommerfeld who first investigated the problem of a surface wave traveling along a cylindrical conductor. For the problem of an infinitely long cylindrical conductor embedded in an infinite homogeneous dielectric, an analytic solution to Maxwell's equations can be found to be:

$$\mathbf{E}(\mathbf{R}, t) = [E_r(r) + E_z(r)]e^{i(kz - \omega t)} \quad (3)$$

$$\mathbf{B}(\mathbf{R}, z) = B_\phi(r)e^{i(kz - \omega t)} \quad (4)$$

Note that both of these fields have azimuthal symmetry (have no dependence on ϕ), thus in the transverse plane the electric field only has a radial component and the magnetic field has only an azimuthal component, resulting in fields as shown on the right in Figure 3. Such a field is said to be *radially* polarized, since the electric field points in a radial

direction at all points along the cylinder. Using the universal wave equation, one can find $E_z(r)$ in equation (3) to be:

$$E_z(r) = \begin{cases} E_c I_0(\beta_c r) & r < R \\ E_a K_0(\beta_a r) & r > R \end{cases} \quad (5)$$

where I_0 and K_0 are the first order modified Bessel functions. Our β coefficients obey the relation:

$$\beta_a^2 - \beta_c^2 = (\epsilon_r \mu_r - 1) \frac{\omega^2}{c^2} \quad (6)$$

where ϵ and μ are the permittivity and permeability constants associated with the respective mediums (and thus are a function of r) and ω is the angular frequency of the radiation. Because E_z is represented by a modified Bessel function, it decays rapidly away from the surface of the conductor resulting in a very small area of strong field distribution. Also note that E_z does not depend on the distance traveled along the conductor, meaning that the wave travels across the surface with zero attenuation (in this theoretical model, at least). Though the use of the condition that our two E_z 's must equal one another at the boundary $r = R$ the components E_r and B_ϕ may also be found:

$$E_r(r) = \frac{k}{i\beta^2} \frac{dE_z(r)}{dr} \quad (7)$$

$$B_\phi(r) = \frac{k^2 - \beta^2}{i\omega\beta^2} \frac{dE_z(r)}{dr} \quad (8)$$

where k is the wavenumber and (using the recurrence relations of the modified Bessel functions):

$$\frac{dE_z(r)}{dr} = \begin{cases} \beta_c E_c I_1(\beta_c r) & r < R \\ -\beta_a E_a K_1(\beta_a r) & r > R \end{cases} \quad (9)$$

since the other components of the magnetic and electric fields are also represented by modified Bessel functions (in this case of first order) they also decay rapidly away from the surface of the conductor.

It is interesting to note that historically it was long debated whether or not Sommerfeld's surface wave actually existed; since the solution requires an infinitely long conductor and an incident plane wave (in other words a radiation source infinitely far away from the surface of the conductor). It was shown experimentally in the 1940s that these types of surface modes could actually be excited in a finite conductor, and Gobau proposed their potential application as transmission lines¹², but only recently have experiments been carried out to investigate this potential in the context of sub-mm waves. Since there are no closed form analytic solutions for the problem of surface waves on a cylindrical conductor of finite length numerical simulations must be carried out to get an

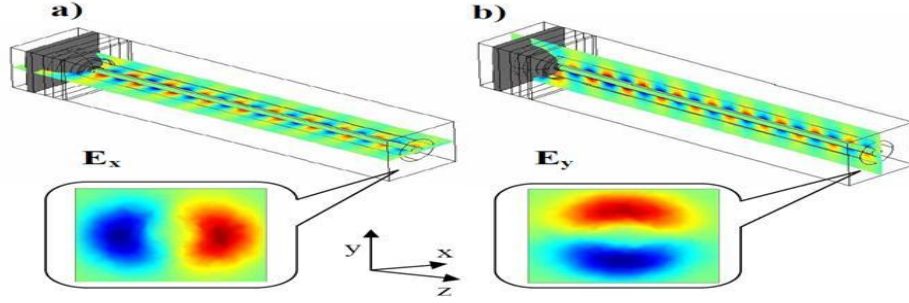


Figure 4: FEM simulation of the electric field of a SPP mode traveling along a conductor of finite length¹⁴. Close-ups of the x and y components of the field are shown. Compare these shapes with the experimental results shown in Figure 18, keeping in mind that our detector measures power (E^2) and is thus not sensitive to the phase of the outgoing wave (shown as red and blue in the simulation).

idea of what such a field should look like. In the case of sub-mm waves the field is found to exist almost entirely on the outside of the conductor ($r > R$) because of the high attenuation sensitivity of the band to metals (penetration depth for the field is less than $1\mu\text{m}$), and the field only extends several mm (depending on wavelength and the waveguide diameter) off the wire's surface. Figure 4 shows an example of one such simulation and the resulting field shape, using these results and through understanding the theory behind Sommerfeld waves we were able to characterize the radiation patterns in our experiment and confirm the presence of SPP modes.

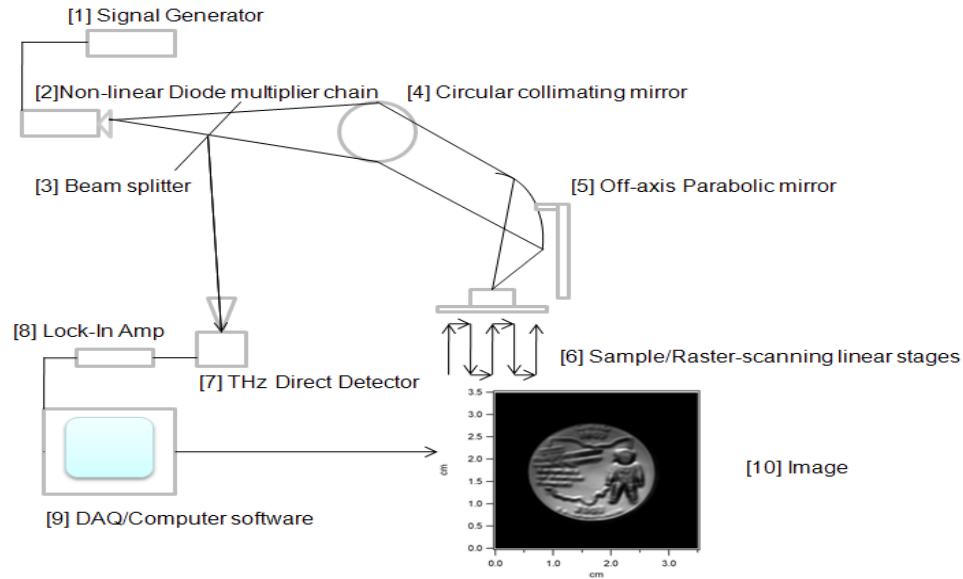


Figure 5: Schematic diagram of imaging system. Radiation exits the multiplier chain and is focused on our raster-scanned sample.

The scattered radiation is then sent to a direct detector, which monitors the reflected power.

2.4 CW Sub-mm Wave Imaging Procedure

The basic theory behind sub-mm wave imaging is no different than that of any other imaging system. In an active system, radiation is sent from the source through a series of optics to illuminate the target, which then reflects and scatters radiation into a detector which composites the image. In our set up the source was the previously mentioned diode multiplier chain, and an output frequency of 610 GHz was chosen due to the fact that it was the highest output power the system was capable of according to the spec data provided by the manufacturer (0.8mW). Our optics consisted of a circular collimating mirror, a 50/50 Mylar beam splitter, and a 90 degree off-axis parabolic mirror with a 4 inch diameter and a 6 inch reflected effective focal length. The off-axis mirror was

chosen due to its low f-number, and was a crucial component in enabling the production of high resolution images. The reflected/scattered radiation off the sample then went back through the optics and half the radiation reflected off the beam-splitter into our direct detector, which was in turn connected to our lock-in amplifier. The lock-in then sent the amplified signal to a National Instruments data acquisition (DAQ) board which was connected to our computer software program. This series of steps enabled the creation of a single pixel in the final image, to produce a full image the technique of raster-scanning was employed as the final step.

Raster-scanning is a rectangular pattern of image capture and reconstruction commonly employed in a variety of imaging applications including television and computer bitmaps¹⁹. It involves a pattern of movement as illustrated in Figure 5 section [6], where the detector, source, or sample (depending on the configuration) is moved pixel by pixel across the entire image area first in one dimension, then moved over in the second dimension by one pixel, then back in the first dimension in the opposite direction, repeated until the entire image area is covered. It allows for the efficient collection and processing of the desired image, and in our case was accomplished through the use of motorized linear stages. Our samples were placed on the stages which were controlled by the same software involved in the collection of data from the DAQ and were moved in a raster pattern, with a time delay between each movement equal to the step size divided by the stage velocity plus two lock-in time constants to ensure that the pixel measurement was averaged and collected before the next move was made. Once the scan was finished the stages then moved back to their initial position to prepare for another image to be taken. The process took approximately 45 minutes for a 20×20 cm image with a

resolution of 0.1mm, the long time due to the fact that our detection scheme only allowed the imaging of a single pixel at a time. To help keep this data collection time at a minimum the stages were set to move at their maximum velocity and our step sizes were set equal to the desired resolution, while these measures did make images quicker to obtain they resulted in several issues which had to be dealt with in image processing.

2.5 Wire Waveguide Procedure

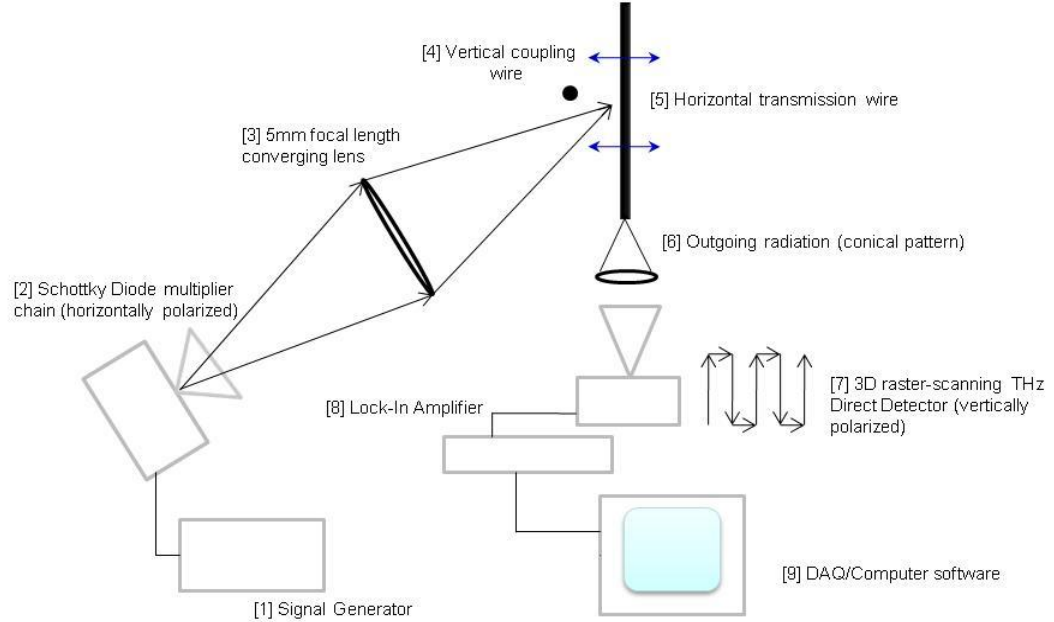


Figure 6: Schematic diagram of wire waveguide system. Outgoing radiation is focused on the gap between the vertical coupling wire and the horizontal transmission wire, exciting the SPP modes. The outgoing conical radiation pattern off the end of the transmission wire is then imaged by 3D raster-scanning the detector, which is mounted on linear stages.

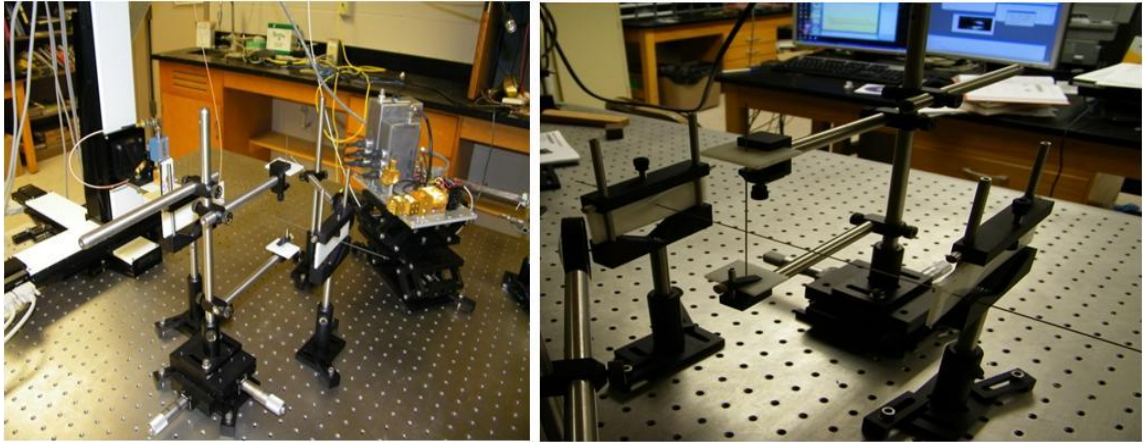


Figure 7: Photographs of the wire waveguide experimental apparatus. Note how the detector is mounted to the linear stages in the left of the first picture, and how the vertical coupling wire is mounted to a micrometer stage to allow for easy manipulation of its position with respect to the transmission wire. The white material (polyethylene) was chosen to hold the wires in place due to the fact that it is largely transparent in the sub-mm wave regime.

The arrangement for the wire waveguide involved a similar design to our imaging experiments, the same signal generator and schottky diode chain was used as in the previous section, and a free standing 5mm focal length converging lens was used to focus the outgoing radiation on our waveguide. The waveguide consisted of two 1 mm diameter tungsten wires, arranged perpendicularly to one another as shown in Figure 6, with a separation distance of approximately 2mm. In addition our initial experiments were carried out with copper wire of various diameters to establish that the radial modes were being excited; we found, however, that although we were able to achieve greater signal strength (approximately three times as much) due to the copper's larger conductivity (copper has a conductivity three times as large as tungsten) the fact that the copper wire

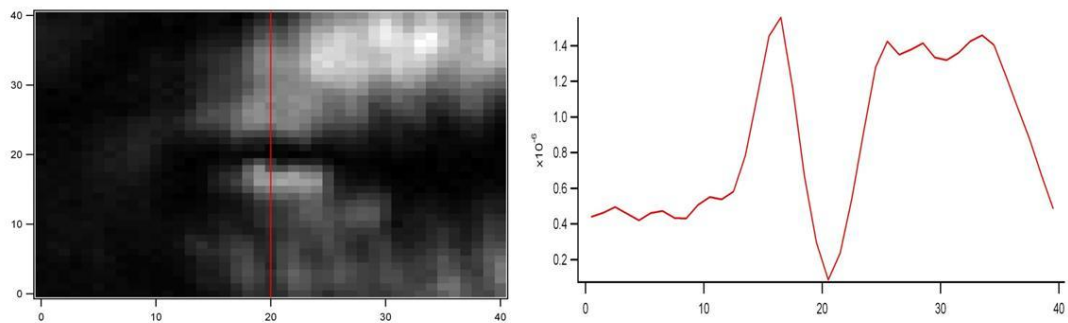


Figure 8: Initial results of waveguide experiment using copper wire, image of outgoing wave and corresponding line profile.

Although the general shape is somewhat visible, the symmetry and distribution of the pattern is irregular due to the uneven surface of the copper wire.

The surface was easily bent and thus made non-cylindrical, greatly affecting the symmetry of the outgoing wave, resulting in images as depicted in Figure 8. Thus tungsten was chosen due to its high tensile strength which allowed the wires to maintain their cylindrical geometry even after being moved and adjusted.

By focusing the linearly polarized radiation (horizontal with respect to the wire in this case) at the gap between the two wires a scattering effect at the intersection structure was created that helped to excite a propagating radially polarized SPP mode²⁰. Although it is possible to excite SPP modes without a coupling wire, the coupling efficiencies of such an arrangement are extremely low (around 0.01%), by utilizing a second wire we were able to couple more of our incident radiation to the desired mode leading to a stronger detectable signal, with coupling efficiency on the order of 1%. This excitation then propagated in both directions away from the intersection down the wire with minimal attenuation due to the transmission efficiency inherent for these modes, and when the radiation reached the end of the wire it diffracted into free space in a conical pattern.²¹ This radiation pattern was then imaged by the same direct detector used in the previous experiment, only this time the detector was mounted on a series of three linear stages allowing for full 3D motion. The detector was aligned to only detect radiation of vertical polarization to minimize noise from back-scattered radiation off the various metal surfaces present in the lab, since the source was polarized in the perpendicular orientation. Also, since the radial field extends several millimeters off of the surface of the wire, we had to be very careful in positioning and mounting to ensure that as little contact as possible was made with the wire surface. To accomplish this wire stands were constructed using high-density polyethylene (a substance largely transparent in the sub-mm wave band) with small drilled holes the same diameter of the wire to hold the wire and keep it straight, as illustrated in Figure 7. In addition, a micrometer stage was built to hold the vertical coupling wire with polyethylene and allow for small adjustments in the coupling wire's position to be obtained with ease since we found that the positioning of

the coupling wire was crucial in obtaining a strong outgoing signal. Both the distance of the coupling wire from the transmission wire and its orientation had to be minutely controlled, and we found experimentally that a distance of approximately 2mm and perpendicular orientation resulted in the strongest, symmetric signal.

By performing 3D raster-scans the outgoing radiation could be imaged in a similar fashion to the NDE images, although in this case since our data was 3D a different software program was necessary to produce graphs. Due to the radial nature of the propagating modes and the fact that our detector was linearly polarized we were unable to image the entire pattern with this set-up. However the majority of the pattern was still imageable since any radiation with polarization not exactly orthogonal with our detector still has some component which is detectable. Once the data was collected it was arranged into 3D matrices and plotted using Igor Pro software which allowed for the easy creation and manipulation of graphs.

Once we were confident that we were in fact imaging the outgoing radial wave several adjustments were made to the setup to see the effects of various parameters. Previous groups have established using numerical simulations and experiments with time-domain systems that the outgoing wave pattern of the wire waveguide widens with decreasing frequency due to near-field diffraction effects at the wire/air interface²². To test these simulations the output frequency of the source was adjusted starting with our initial frequency of 610 GHz and ranging from 580 to 655 GHz and the outgoing wave was imaged at the same distance from the wire in all three cases (5 millimeters). Though the change in frequency was small it was still large enough to notice the diffraction effect, and 3D plots of the data were generated this time with the third dimension being

frequency instead of distance from the wire. In addition to investigating the effects of changing frequency on the outgoing radiation pattern, we placed a third tungsten wire near the far (non-imaged) end of the transmission wire to see what effects this would have on the pattern on the opposite side. The lack of both experimental and theoretical information on the interaction of the two outgoing waves propagating along the waveguide was one motivation for this experiment. It was also our hope that some sort of noticeable effect would be created by back-scattering radiation off the free standing wire with potential application in a sub-mm wave microscopy device. By placing a free standing wire 5 millimeters above and below the far end of the transmission wire we were able to see the effects of a conductive surface placed within the outgoing field of the emitted radiation pattern on the opposite side and evaluate the potential of such an arrangement as a near-field imaging device.

2.6 Software Control

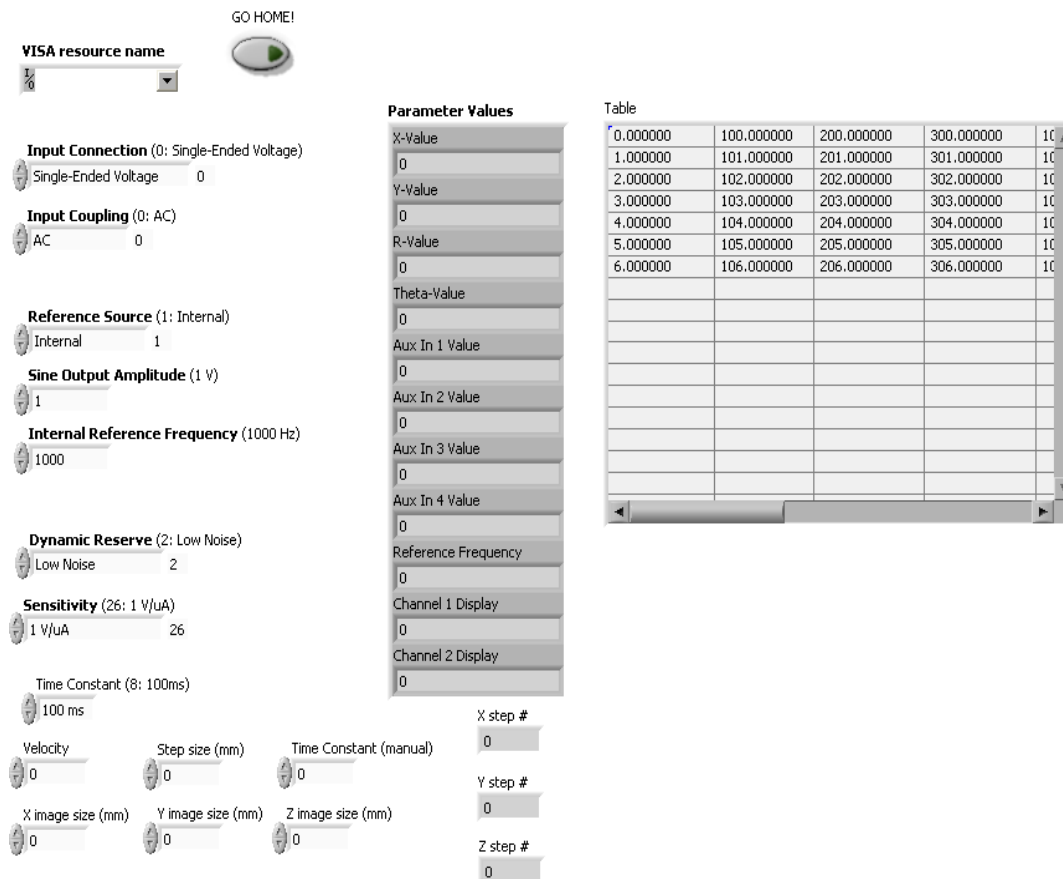


Figure 9: Front panel of LabView software for imaging programs. Panel allows the control of all lock-in parameters as well as image size and stage velocity. Data from the lock-in is collected and displayed in the tables on the right

One of the most crucial components in the design of our experimental systems was the utilization of software to control the motorized stages the samples/detector were placed on and synchronize this motion with our data collection. To achieve high resolution our images often consisted of 22,000 data points or more, and each of these data points had to be correctly timed with the movement of the stages in order to composite an accurate image. To achieve this, National Instruments' LabView software was utilized due to LabView's well documented capability for device control²³. We

found that although LabView did make instrument control and data synchronization easy, its image processing functions left a lot to be desired, thus LabView was used strictly for control and data collection while image processing was achieved using Igor Pro.

To accurately control our systems, the raster-scan logic loops sent to our motion control stages were synchronized with our data collection off of the DAQ board. To minimize the effects of noise and other perturbances on the intensity measurements, data from the lock-in was averaged over 100 measurements made at a rate of 1 kHz for each pixel to increase the effective time constant. Once the data was collected, commands would be sent to the stages to move them over to the next data point. To ensure that the data collected for the next pixel would not be effected by the previous measurement, the system would then wait several lock-in time constants (with $\tau = 100$ milliseconds) before making the subsequent measurement to ensure that the amplifier had enough time to adjust to the new position. Although these measures did lengthen our data collection time by several minutes, we found through trial and error that they were necessary in order to create high quality, reproduceable images. Once the scan was completed the data was arranged into a matrix by LabView, with the rows and columns of the matrix corresponding to the spatial coordinates of the imaged pixel. These matrices were then saved as an external text file, which could then be copied into an Excel spreadsheet for use in our image processing software.

2.7 Image Processing

Once raw data was obtained by the collection software image processing tools were utilized to create our final results. The matrices corresponding to the images were loaded into Igor Pro, and an initial image was generated via the software in order to produce an image more pleasing to the eye. Many of our initial images suffered from the problem of shift register, caused by inconsistencies in the synchronization of the data collection from the lock-in and the raster motion of the stages. Although this problem was eventually corrected for by improving the LabView synchronization programming, shift registering had an important effect on a number of the images in our library. This caused the rows in the data matrix to be shifted, resulting in

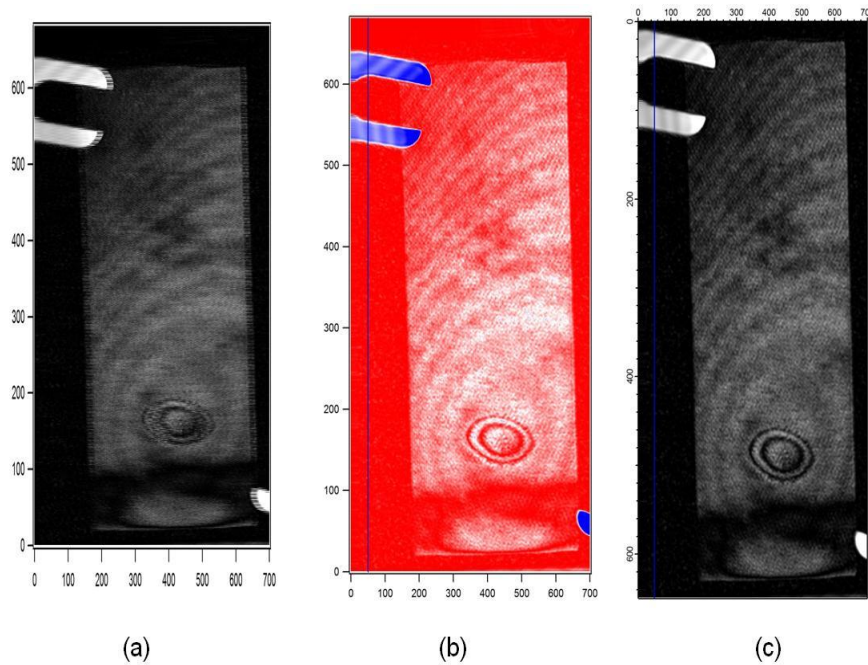


Figure 10: Example of image processing on polyamide sample. Figure (a) depicts the raw data, the effects of the register shift can be seen clearly on the edges of objects. Figure (b) depicts object after register correction. Figure (c) depicts the final image after interpolation, with smooths the appearance of the image noticeably.

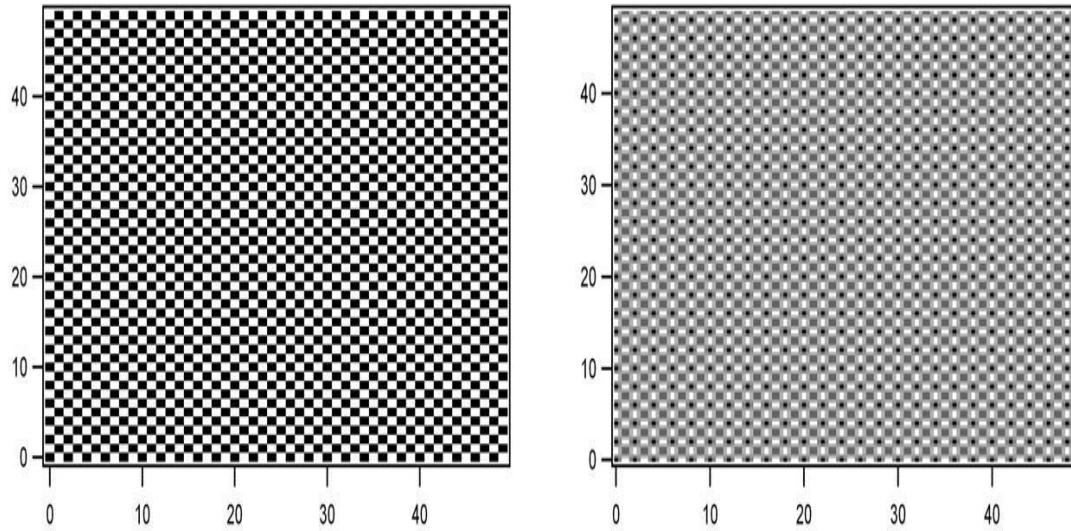


Figure 11: Graphs illustrating the effect of bilinear interpolation on a checkerboard pattern. The image to the left is the raw data, and the figure on the right depicts the interpolated image. Interpolation creates a grey-scale between the dark and white squares in all directions due to the averaging nature of bilinear interpolation.

images as shown in Figure 10 (a). To solve this problem we used Igor to manually move the columns around until a satisfactorily lined up image was produced, as shown in Figure 10(b).

The final step of our image processing involved a technique known as interpolation. Interpolation is the mathematical method of constructing new data points within the range of discrete set of known data points, and is a commonly used technique in image processing²⁴. Through interpolation new pixels are constructed by linearly averaging the pixels in the surrounding area, then inserting a new pixel with a value equal to this average. This method is known as bilinear interpolation, and its effects are illustrated in Figure 11. The net effect is an overall smoothing of the image appearance;

although averaging does slightly decrease our effective resolution the increased clarity makes the identification of small defects easier to the human eye. We utilized interpolation for two reasons; one, it allowed us to increase the step size of our linear stages during imaging greatly reducing data collection time and second, it allowed sub-resolution interference effects to be smoothed making defects and other items of interest easier to see with the naked eye. Once the data was interpolated and we were satisfied with the appearance of the image the files were converted into JPEGs and exported. Through the use of image processing we were able to convert our less than ideal raw data into images of picture quality, allowing for easier evaluation of the structures we sought to find.

III. NDE Imaging Results

3.1 Evaluation of Metallic Samples

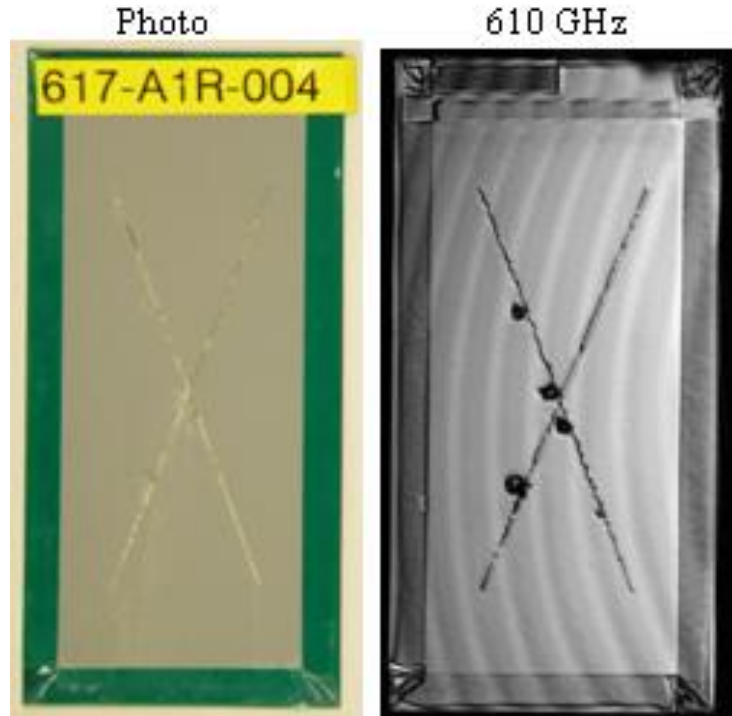


Figure 12: Visual and sub-mm wave images of corrosion sample A1R-004. Blistering underneath the paint is slightly visible in the photo but shows up clearly in the 610GHz image due to scattering. The interference patterns in the sub-mm image are due to multiple reflections within the system and not an error caused by image processing.

The first set of samples we imaged were aluminum sheets 3" \times 6" in size with either half or all of the sample covered with a paint layer approximately 0.1mm thick to serve as an obscurant. Each sample had a large 'x' shaped score mark and was subjected to a series of chemical treatments to help initiate the growth of corrosion resulting in blistering, pitting, and cracking of the metal and paint surfaces. These surface defects

show up very clearly in the sub-mm images due to scattering, as illustrated in Figure 12, but are typically barely visible in the photos. The interference bands seen in the sub-mm wave image are due to the highly coherent nature of our source, near field effects, and multiple reflections within the system, creating an arrangement not unlike a Michelson interferometer resulting in interference fringers. Although these fringes result in less than ideal images, they can also aid in locating defects and other areas where the refractive index changes as the fringe patterns warp around these areas. There are several methods that could be implemented in future efforts to eliminate these effects, for example frequency modulation²⁵

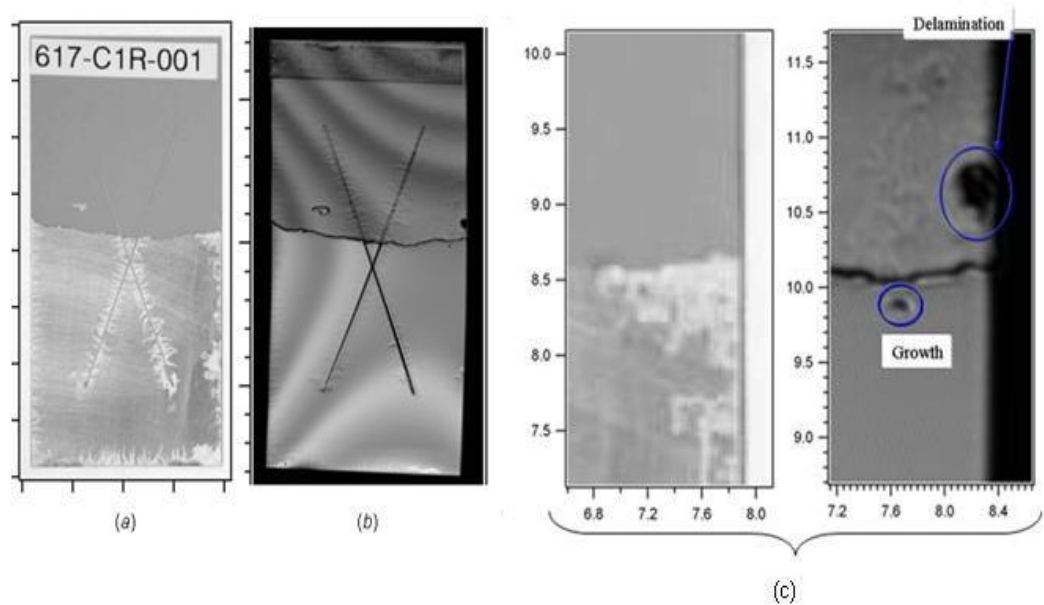


Figure 13: Visual and sub-mm wave image of corrosion sample C1R-001. (a) and (b) are the full visual and 610GHz images, respectively. (c) shows a closeup of the right side of the sample, illustrating defects seen in the sub-mm image but not in the visual and vise-versa.

One good illustration of this effect is in our image of metallic sample C1R-001. Here a definite change of the interference bands can be seen between the metal and paint areas, and the bands shift around the delamination on the right side as well as some of the

vein like growths along the central score mark. This image also shows the kind of defects that show up clearly in the sub-mm image and vise-versa. While the vein-like corrosion structures show up clearly along the 'x' shaped score mark, they are not as apparent on the edges of the sample in the 610 GHz image. This is likely due to the structures' small thickness (0.1mm or less) and the high intensity of the signal reflected off the surface of the bare metal washing out the small change in signal. On the other hand growths and delaminations underneath the paint layer, as shown in the close-up in Figure 13(c), are clearly visible in the sub-mm wave images but virtually undetectable in the visible photo. Thus, it appears that the sub-mm wave imaging system is better at finding defects underneath the paint layer than it is on the bare-metal surface. However, since the defects on the metal surface are clearly visible this is not a significant disadvantage, since any routine NDE inspection would include a visual overview as well as imaging.

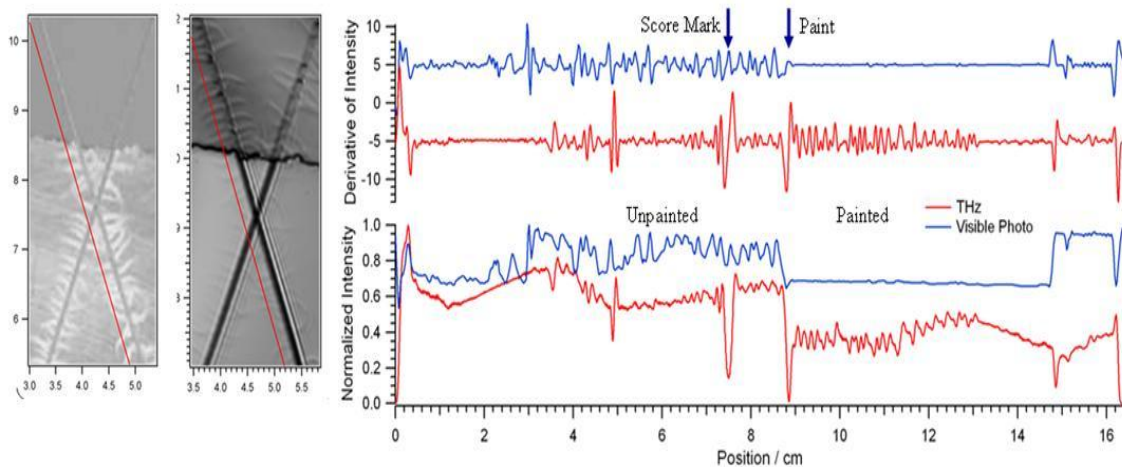


Figure 14: Line profiles of visible and sub-mm wave images of sample C1R-001 (taken along red line shown in images on right. To offset the effects of the interference fringes, the intensity pattern's normalized and derivative values are plotted.

To get a more quantitative evaluation of these images, we utilized line profiles. Because the interference patterns in the sub-mm wave images direct intensity comparisons are not very useful, we plot in Figure 14 the normalized intensity distribution as well as its derivative for the visual and sub-mm wave images. From the line profiles, several features of the images can be determined, first in both the sub-mm and visible images the regions of high contrast show a 10-15% variation in intensity while areas of low contrast (such as the paint layer in the visual image) show virtually no variation. Second, while the paint layer barely registers in the visible image stark contrast can be seen in the sub-mm wave profile, illustrating the penetrative capabilities of this wavelength. Third, variations in the surface such as the score mark and vein-like growths cause a greater change in intensity in the sub-mm wave image than in the visible, most likely due to the fact that the 610GHz wavelength is closer to the size of the defects and is thus affected by Mie-Debye scattering more than optical frequencies. Finally, the profiles illustrate how in the metal region many of the features are lost in the sub-mm wave image but are still distinct in the visible, showing that the 610GHz system is better suited for finding defects underneath paint than on a bare surface, but this will be determined by the defect size and the geometry of the target.

3.2 Evaluation of Composite Samples

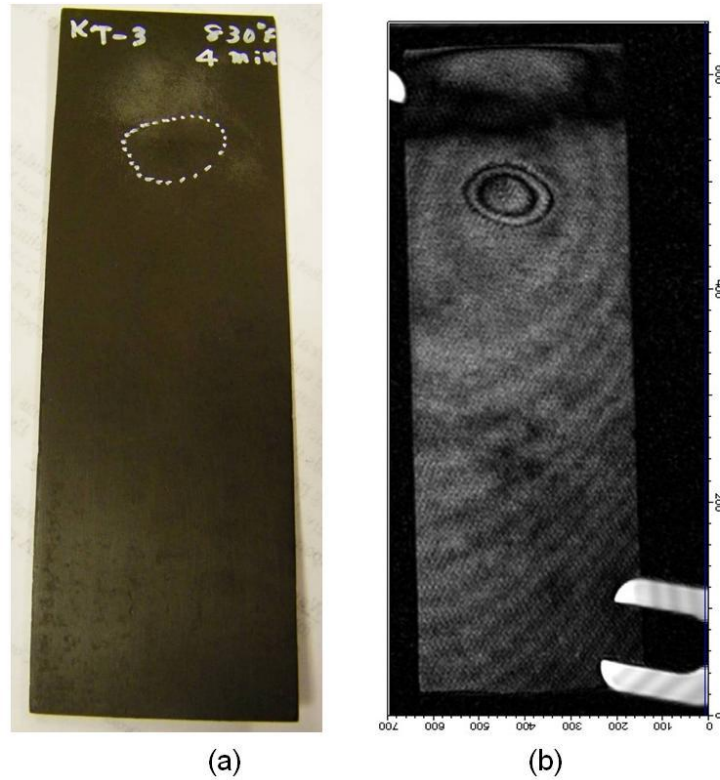


Figure 15: Visible (a) and 610GHz (b) image of composite sample KT-3. Sample was burned for 4 minutes at 830 degrees F, as labeled. The burn spot shows up clearly in the sub-mm wave images, while being indistinguishable in the visible.

The second set of samples we evaluated were fiberglass/polyamide areospace composites approximately 2''x 6'' in size and 5 millimeters thick. These samples had a variety of different defects including burn damage, stress damage, and hidden delaminations purposefully manufactured to test our instruments. Figure 15 shows a sample that had an area (outlined in white in the photo) subjected to 440 °C for a 4 minute duration resulting in structural damage and delamination of the component composite material. Although the damaged area does not appear significantly altered in the visible photograph the burn spot can be clearly seen in the 610GHz image, and indeed this kind

of structural damage could lead to component failure if experienced in the field. Once again we see the interference patterns due to near field effects as well as multiple reflections in our system. In addition we are able to make out the honeycomb weave structure of the material which is not visible to the naked eye.

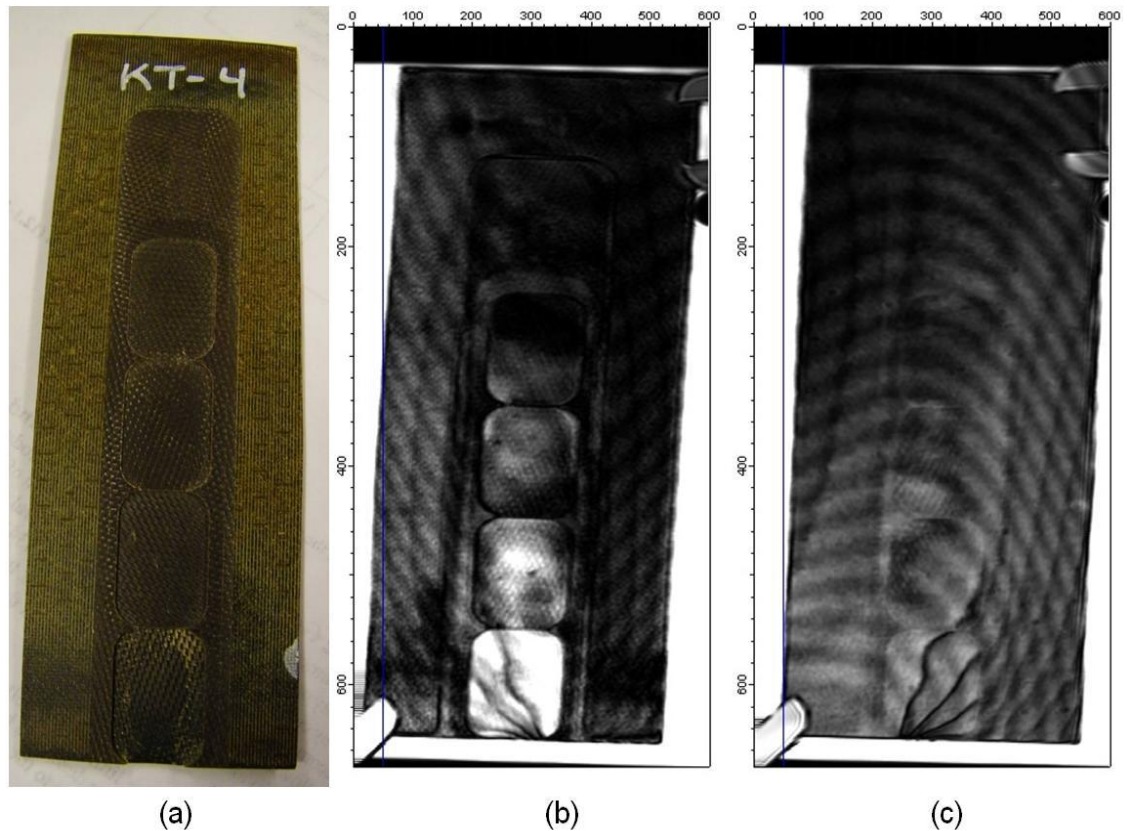


Figure 16: Images of composite sample KT-4, visual (a) front (b) and back(c). Sample was bent at a rate of 60Hz for five minutes, the effects of the stress damage can clearly be seen as fold-like structures in the image and are not visible in the photo.

Figure 16 depicts another of our composite samples and this one has several interesting features compared to the previous one. First the center of the sample has had varying thicknesses carved out (approximately 0.5-2 millimeters in depth) in order to test the effect of different declinations on our images, in addition this sample was subjected to stress damage instead of being burned and the effects are unnoticeable in the visible. In

the 610 GHz images, however, the effects of the stress damage are clear in the lower corner of the image, the fractured layers can clearly been seen on the back side of the composite and somewhat on the front side through the thinnest layer. This type of stress damage could result in component failure if unmonitored and again illustrates the capabilities of our system for NDE.

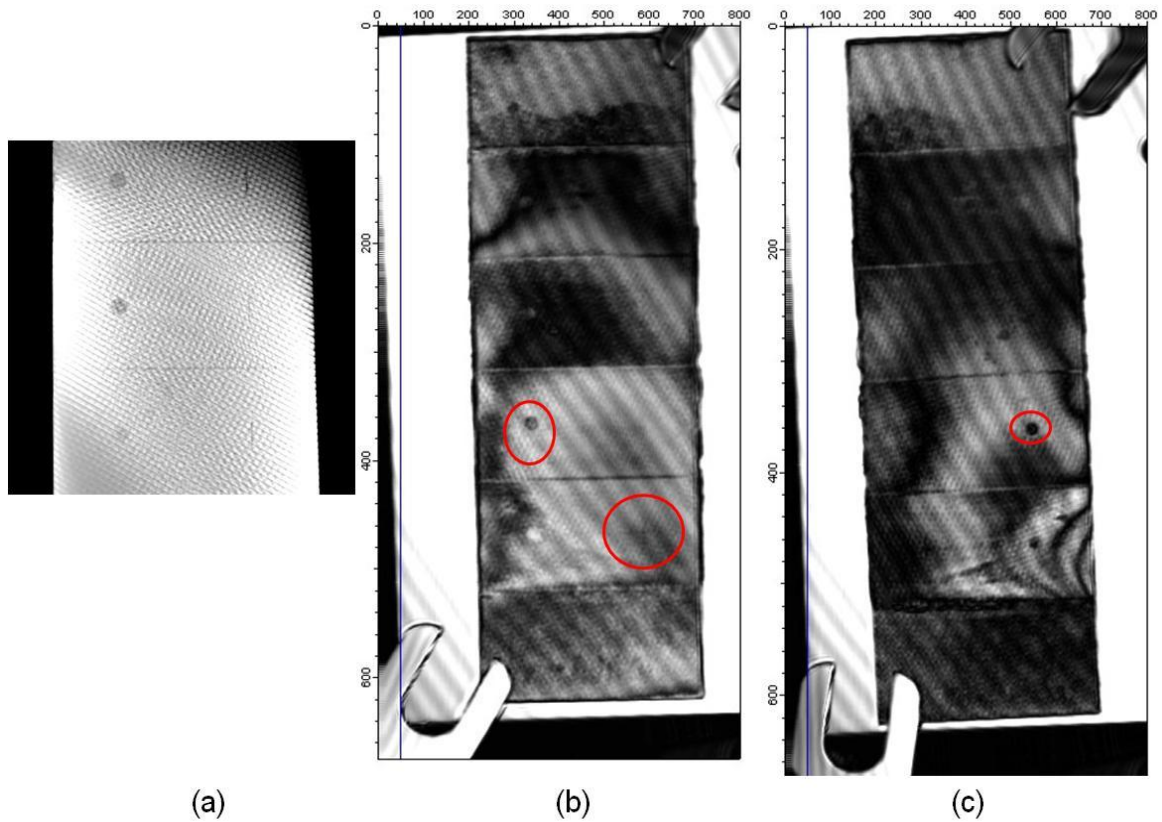


Figure 17: Image of hidden defects in composite sample NKT-4. (a) X-ray image²⁶ (b) and (c) sub-mm wave images of the front and back of the sample, respectively. The circular and horizontal line defects are clearly visible but the vertical line defects barely register in the 610GHz pictures.

The most interesting of our composite samples is shown in Figure 17. On the surface, this sample appears plain and unmarred but in fact has had hidden delaminations

purposefully introduced within the weave structure. As the X-ray image in Figure 17 (a) shows, there are circular as well as vertical and horizontal line defects present within the sample. The circular and horizontal line defects show up clearly on the front of the sample in the 610 GHz images, and less clearly on the back, the vertical line defects are unfortunately not as clear. These line defects are much less than 1 millimeter in width, and they are pushing the resolution limit of our system. However, one appears to be noticeable in the right red circled region in Figure 17 (b). What is even more interesting is a direct comparison between our images and the X-ray one. We seem to get about the same spatial resolution even though the X-rays have wavelengths orders of magnitude smaller (and are of course ionizing and therefore has limited field capabilities). As composite materials become more and more popular in aviation, their effective evaluation becomes more and more crucial, and these images demonstrate that sub-mm waves are not only capable of evaluating surface damage in metals but the interior of composite materials as well.

IV. Sommerfeld-Zenneck Waveguide Results

4.1 Initial Measurements and Efficiency of Coupling Wire

Our first goal after constructing our wire waveguide was to confirm that we were indeed exciting the SPP modes of the conductor and that the output radiation we were measuring was the conical wave pattern we sought to image. To accomplish this we manually moved the stages around the wire to get an idea of where the intensity peaks were located with respect to the end of the wire, and that these positions correlated with what would be expected from a SPP mode. Once a region of maximum intensity was located we would move the detector to the opposite orientation with respect to the transmission wire to make sure that the intensity distribution was symmetric. What we found was that the symmetry of intensities was greatly dependent on the position of the coupling wire; if the coupling wire was not perfectly perpendicular to the transmission wire an asymmetry would result. In addition the signal strength would change as the distance between the coupling and transmission wires was adjusted, increasing at first as the wire was moved back and then steadily decreasing as the wire was moved further and further away. We found that a separation distance of approximately 2mm was optimum for maximum signal strength and symmetry.

In addition to confirming the presence of an outgoing SPP mode we calculated coupling efficiency of the wire waveguide to confirm that we were not seeing stray reflections and to confirm that our efficiencies corresponded to those found by previous groups²⁷. Our maximum output was approximately 1.3 μV as read by our lock in, which

corresponded to a detected power of approximately $.001\mu\text{W}$. If we assume this power corresponds to an area of $.01\text{ mm}^2$ (the area of the pixel for a $.1\text{mm}$ step size) and use the fact that the average radius of our radiation pattern immediately exiting the end of the waveguide was approximately 2.5mm , we can estimate the coupling efficiency. A radius of 2.5mm results in a total surface area of approximately 20mm^2 , assuming the total power distribution is uniform (which it should be according to theory) this means that the total power of the radiation pattern was approximately $2\mu\text{W}$. Given that the output power of our source is 0.8 mW at 610 GHz (see Figure 2) this gives us a coupling efficiency of approximately 0.25% , which corresponds to the efficiencies seen by other groups researching these waveguides, taking into account losses due to attenuation and other effects. Although the coupling efficiency for this waveguide is extremely small there is very little attenuation over the length of the wire. Approximately the same signal strength was seen with wire lengths of 70 cm as was seen in lengths of 35 cm . In addition, due to the sensitivity of our detectors even such a small amount of radiation is still sufficient to use for imaging applications. Once these initial measurements were complete our next task was to quantify the parameters of the outgoing wave on the far end of the waveguide.

4.2 Evaluation of Outgoing Wave as a Function of Distance

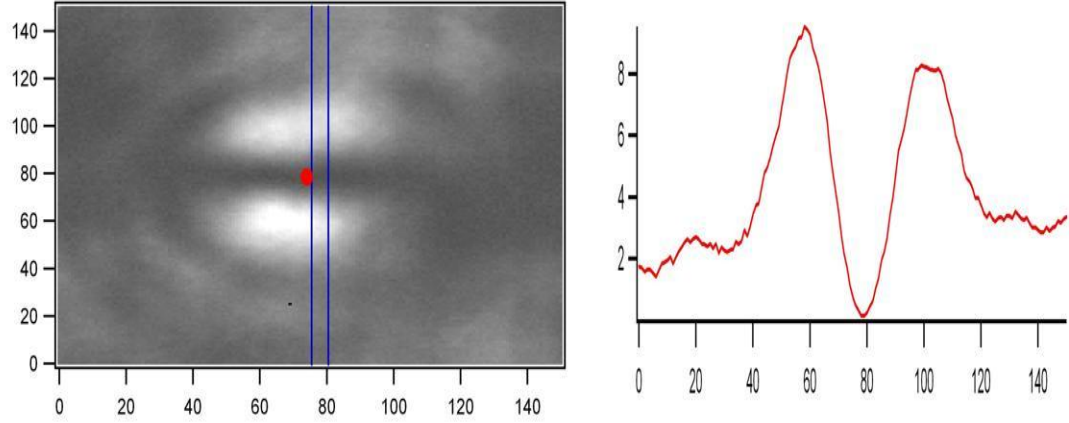


Figure 18: 2D image of outgoing wave at 610 GHz and corresponding line profile (taken between blue lines), the detector was placed 13 mm from the tip of the transmission wire, and each unit in the graph is equal to 0.1 mm. Notice the strong intensity in the immediate vicinity of the wire (red circle) and the less intense outgoing wave pattern surrounding it. Also note that there is no intensity to immediate the left or right of the wire, since our detector is polarized in the vertical direction.

By performing our 3D raster-scans, in effect a form of terahertz tomography²⁸, we were able to evaluate the outgoing wave pattern as a function of distance from the wire and compare our results with those predicted by theory. Figure 18 depicts a 2D section of our 3D data along with a corresponding line profile. Notice that we get an almost circular pattern, as we would expect as a section of our conical outgoing wave, but that there is no intensity to the immediate left or right of the wire. This is due to the nature of the SPP mode's radial polarization, since our detector is linearly polarized in the vertical direction it is unable to detect the outgoing radiation with polarization perpendicular to this axis. Also, the intensity pattern is symmetric about the wire, although the intensity peaks

slightly higher above the wire than below. This is most likely due to a slight perturbation of the position of coupling wire, which as noted before can lead to asymmetries in the outgoing wave pattern.

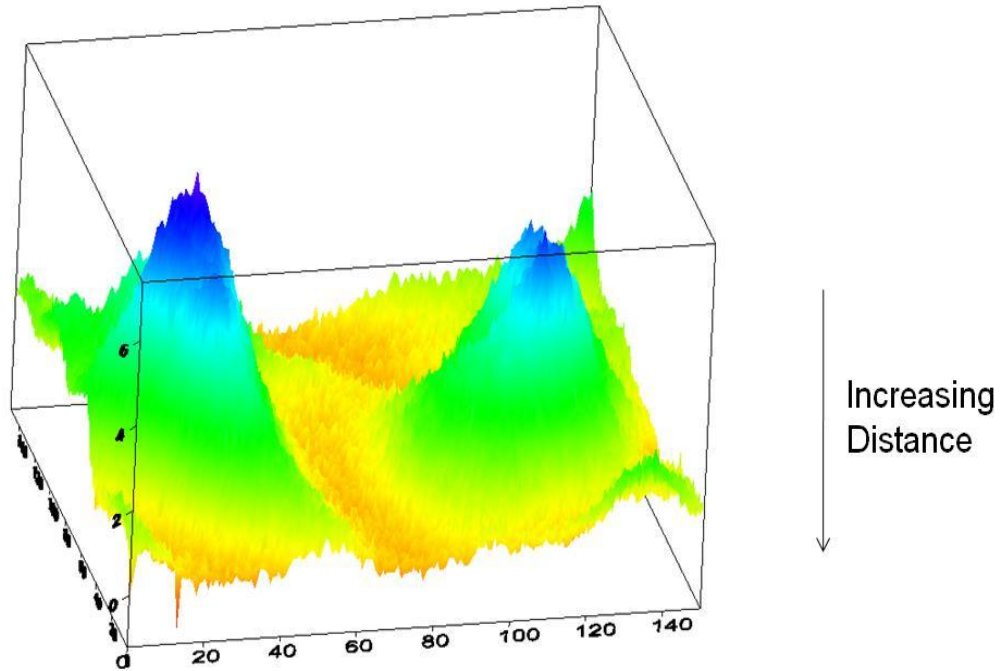


Figure 19: 3D image plot of outgoing intensity versus distance. Imaging began at 5mm and tomographs were taken every 8mm back as far as 45mm. Notice the conical shapes of both halves of the radiation pattern and the noise level intensity for positions perpendicular to the polarization of the detector.

Figure 19 depicts the 3D graph of the outgoing radiation pattern as a function of distance from the wire. Immediately apparent is its conical shape, which correlates well with theory. Once again the asymmetry of the pattern is evident as well, although the differences between the two halves become less pronounced with distance. This brings us to the next point, which is that both halves of the wave pattern diverge from the center at

approximately the same rate, as would be expected of a diffraction pattern in the far-field limit. Figure 20 shows a plot of the peak-to-peak distance of the two halves of the intensity pattern as a function of distance from the tip of the transmission wire, as well as the intensity distributions for six different distances (essentially 2D tomograms of our 3D plot). This linear behavior is indicative of the diffraction effects at the wire/air interface, and is further evidence that the pattern we are viewing is indeed the conical outgoing wave expected from an excited SPP mode on a cylindrical wire waveguide. These results verify that our method of Sommerfeld-Zenneck wave excitation is valid, and that the behavior of the wave correlates well with theory, with the exception of the slight asymmetry between the two halves of the wave pattern.

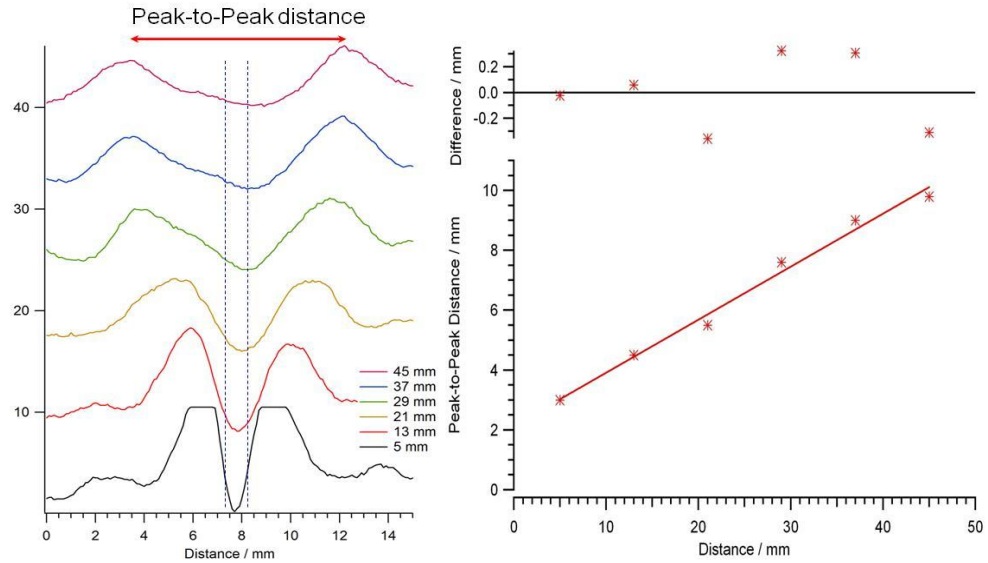


Figure 20: Plot of peak-to-peak distance of outgoing wavefronts as a function of distance from the wire, with deviation shown above. The left plot maps the intensity distribution of the outgoing pattern for 6 different distances, and the right plot shows the relationship between the peak-to-peak distance and distance from the wire. Distances show a linear relationship with position from the wire, as would be expected due to diffraction in the far-field limit.

4.3 Evaluation of Outgoing Wave as a Function of Frequency

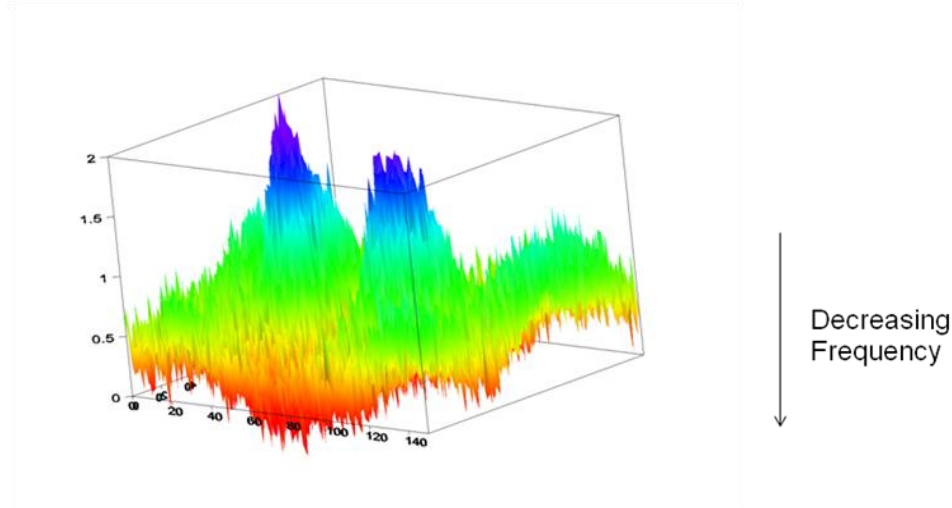


Figure 21: 3D Plot of outgoing wave pattern as a function of frequency. Although the pattern does widen slightly as predicted by frequency-dependent scattering, the high level of noise in our measurements as well as the limited range of frequencies of our source limits conclusiveness of this data.

Our next set of data sought to verify the frequency dependent behavior of the outgoing pattern. Figure 21 shows our 3D plot of the wave pattern as a function of frequency. Although the distance between the peaks did widen slightly (approximately 3mm difference between the 580 and 655 GHz peaks), the results are not thoroughly conclusive. The high level of noise in our 580 GHz measurement, as well as the limited frequency range of our radiation source were both limitations on this aspect of the experiment. Although the small variation in the peak-to-peak distance does correlate with the difference predicted by the simulations performed by previous groups, the fact that we lacked a source/detection scheme broadband enough to make the necessary number of measurements hampered our results considerably.

4.4 Effects of the Presence of Conductors on the Outgoing Wave

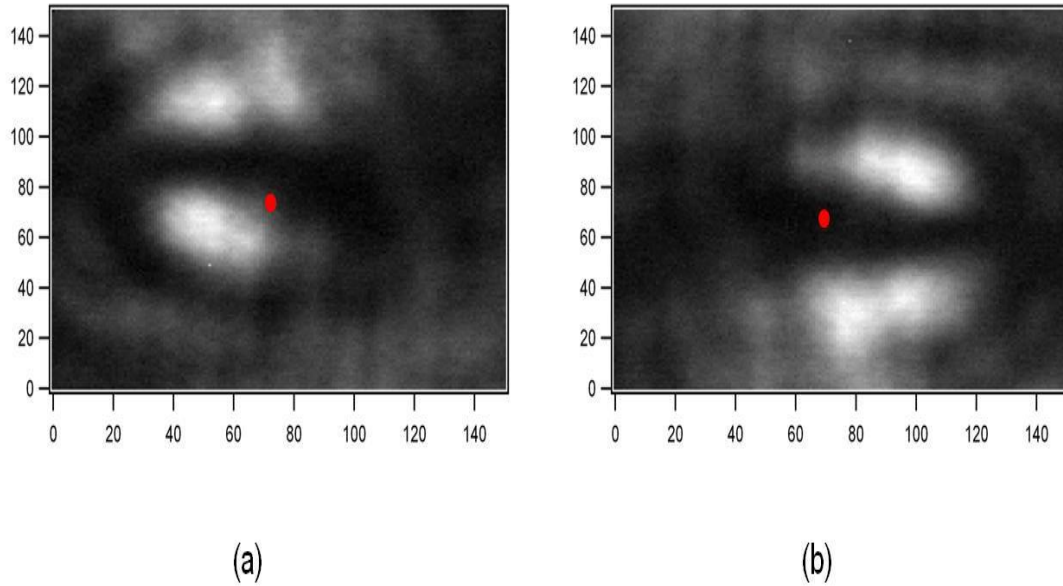


Figure 22: 2D image of outgoing wave at 610 GHz when a second wire is placed (a) 5mm above and (b) 5mm below the far (non imaged) end of the transmission wire (images taken at a distance of 21mm). Note how the symmetry of the pattern is lost and how it is no longer centered on the face of the wire (red dot). Also notice how the two images are almost reversed images of one another.

Our final set of measurements investigated the effects of the presense of a second cylindrical conductor on the outgoing wave. Our resulting images are displayed in Figure 22; notice how the symmetry of our previous images if broken. The outgoing wave appears to be effected by reflections from the far end of the wire resulting in the asymmetric radiation pattern. In addition, the images of the outgoing wave when the wire is place above and below the wire appear to be mirror images of eachother, which again supports the theory that this asymmetry is due to reflections off the far end of the wire (with left-right reversal). While no more detailed analysis of these effects was made,

further investigations of these effects may reveal the potential of such a waveguide to be used for near-field imaging and microscopy, fields where the sub-mm wave band has not been extensively utilized. It also presents evidence that the two outgoing waves generated by our SPP generation scheme do interact with one another; a fact that to this author's knowledge has never been investigated before. Although these measurements are very preliminary, they suggest a new line of inquiry that may further realize the potential of a Sommerfeld-Zenneck waveguide not only as a means of sub-mm wave transmission but as a method of near-field imaging.

V. Conclusions

As the technology for the generation and detection of sub-mm waves becomes more and more advanced it becomes increasingly important to investigate the potential applications and methodology of utilizing this wave band. By constructing our NDE system and creating our library of images we have successfully demonstrated the advantages a sub-mm wavelength device could yield to the maintenance community, and specifically the potential such a system in evaluating aerospace metallic and composite materials. While the results of our NDE experiments are promising, the problem of sub-mm wave transmission still needs to be addressed before a field-capable system can be developed. Our waveguide experiments have shown a potential solution to this issue by demonstrating SPP generation in cylindrical waveguides for the first time using a CW system. While a great deal of research still needs to be carried out before an effective Sommerfeld-Zenneck transmission wire can be realized, our research is a promising step in this direction. Since it has been demonstrated that such a waveguide is capable of transmitting CW sub-mm wave radiation over considerable distances with little attenuation, future research should center on investigating methods for increasing the coupling efficiency of such a device, as proposed by several groups in the research community^{29,30}. Increasing the efficiency of such a waveguide maximizes its potential for practical field use. Such a method of sub-mm wave transmission would not only have potential impact in the field of NDE, but nearly every other application of the band as well.

References

1. "The Terahertz 'Gap'", www.teraphysics.com/newimages/Terahertz%20Gap.jpg, image retrieved August 2009.
2. A.A. Penzias and R.W. Wilson, "A Measurement of Excess Antenna Temperature at 4080 Mc/s", *Astrophysical Journal* **142**, 419-421 (1965).
3. Tonouchi, Masayoshi. "Cutting-edge terahertz technology", *Nature Photonics*, Vol 1, February 2007, pgs. 97-105.
4. Zhang, X.C., Abbott, D., "Scanning the issue: T-Ray imaging, sensing, and retection", *IEEE* Vol. 95, No. 8, August 2007, pgs. 1509-1513.
5. Koch, G.H. "The Cost of corrosion: Aircraft", www.corrosioncost.com/transportation/aircraft/index.htm, retrieved December 2008.
6. Bardal, E., Drugli, J.M., "Corrosion Detection and Diagnosis", *Materials Science and Engineering*, Eolss Publishers, Oxford, UK, 2004.
7. Qing C., Jurgen J., "Azimuthally polarized surface plasmons as effective terahertz waveguides", *Optics Express*, Vol. 13, No. 2, January 2005, pgs. 511-518.
8. Karpowicz, N., Zhang, X.C., et al, "Comparison between pulsed terahertz time-domain imaging and continuous wave terahertz imaging", *Semiconductor Science and Technology*, Vol. 20, 2005, pgs. S293-S299.

9. “Active versus passive sub-mm wave imaging”, Terahertz Optoelectronics
www.sic.rma.ac.be/~rhereman/Thz/book_cha3.pdf, pages 12-20.
10. Meyendorf, N.G.H., Nagy, P.B., Rokhlin, S.I., Nondestructive Materials Characterization with Applications to Aerospace Materials, Springer Scientific Press, New York, 2003.
11. A. Sommerfeld, Ann. Physc. U. Chemie (Neue Folge) **67-1**, 233 (1899).
12. Goubau, Georg “Surface Waves and Their Application to Transmission Lines”, *Journal of Applied Physics*, Vol. 21, November, 1950, pgs. 1119-1128.
13. Winnerl, Zimmermann, Peter, Schneider, Helm, “Terahertz Bessel-Gauss beams of radial and azimuthal polarization from microstructured photoconductive antennas”, *Optics Express*, Vol. 17, No. 3, February 2009, pgs. 1571-1576.
14. Deibel, J., et al., “Enhanced coupling of terahertz radiation to cylindrical wire waveguides”, *Optics Express*, Vol. 14, No.1, January 2006, pgs. 279-290.
15. Lee, Yun-Shik, Principles of Terahertz Science and Technology, Springer Scientific Press, New York, 2009.
16. “About Lock-in amplifiers”, Technical Manual, SRS Application Note #3, Stanford Research Systems, www.thinkSRS.com, Retrieved August 2008.
17. Simon, B., Reed, M. Scattering Theory (Methods of Mathematical Physics Vol. 3), Academic Press, London, 1979.

18. Kerker, M. The Scattering of Light and other Electromagnetic Radiation, Academic Press: London, 1969.
19. Wootton, Cliff. A Practical Guide to Video and Audio Compressions: From Sprockets and Rasters to Macro Blocks, Focal Press, New York, May 2005.
20. Wang, K., Mittleman, D. “Metal wires for terahertz wave guiding”, *Nature*, Vol. 432, November 2004, pgs. 376-379.
21. Wang, K., Mittleman, D. “Guided propagation of terahertz pulses on metal wires”, *Journal of the Optical Society of America*, Vol.22, No.9, September 2005, pgs. 2001-2008.
22. Deibel, J., et al., “Frequency-dependent radiation patterns emitted by THz plasmons on finite length cylindrical metal wires”, *Optics Express*, Vol.14, No.19, pgs. 8772-8778.
23. Paton, Barry. Sensors, Transducers & Labview, Prentice Hall, New York, 1998.
24. Meijering, Erik (2002), "A chronology of interpolation: from ancient astronomy to modern signal and image processing", *Proceedings of the IEEE* **90** (3): 319–342.
25. Petkie, D., et al., “Active and passive millimeter and sub-millimeter-wave imaging”, proceedings of SPIE Security & Defense Conference 5989C, Bruges, Belgium, Sept. 2005.
26. Stoik, C. D., Bohn, M. J., and Blackshire, J. L., “Nondestructive evaluation of aircraft composites using transmissive terahertz time domain spectroscopy,” *Opt Express*, 16(21), 17039-17051 (2008).

27. Agrawal, A., Nahata, A., “Coupling terahertz radiation onto a metal wire using a subwavelength coaxial aperture”, *Optics Express*, Vol. 15, No.14, July 2007, pgs. 9022-9028.
28. Mittleman, D., Sensing with Terahertz Radiation, Springer Scientific publishing, pgs. 117-150, 2003.
29. Maier, S., et al. “Terahertz surface plasmon-polariton propagation and focusing on periodically corrugated metal wires”, *Physical Review Letters*, Vol. 97, No. 176805, pgs. 1-4, October 2006.
30. Nahata, Ajay, “Terahertz transmission through quasiperiodic arrays of subwavelength apertures”, APS March meeting abstract, <http://meetings.aps.org/link/BAPS.2007.MAR.Y31.2>, retrieved August 2009.